Time-resolved imaging of the energy relaxation

5.1 Introduction

5.1.1 Ultrafast pulses for ultrafast images

In order to follow the course of the changes involved in any dynamic phenomenon, one has to adapt its experimental apparatus depending on how fast the action takes place. For slow phenomena, a natural tool is a camera equipped with a burst mode. Typically, rates of 40 frames per second (fps) can be attained. This means that any event faster than 25 ms can not be resolved. Taking individual pictures lowers the limit down to the minimal exposure time (on the millisecond scale) but is limited by the duration of the mechanical movement of the shutter during opening. In order to avoid mechanical and electrical limitation intrinsic to detection, optical methods are to be used. Based on this principle, strobe photography provides excellent results. The phenomenon to observe is placed in a dark environment, the shutter is opened and a short flash of light is generated. The temporal resolution is then theoretically as short as the flash employed to lighten the recording medium (film or light sensitive matrix). Applying the same method with a femtosecond laser source presumably allows imaging with a subpicosecond resolution.

The phenomenon we want to follow in time is the evolution of the complex refractive index upon excitation with laser fluences relevant for technological applications, i.e. in tight focusing conditions at energies slightly above the permanent modification threshold. The real part of the refractive index is measured by phase contrast microscopy (PCM)
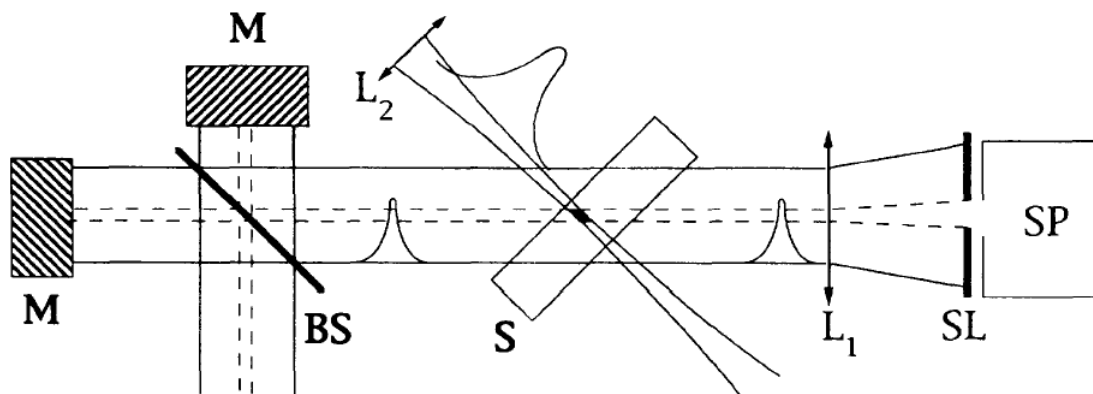
Figure 5.1: Principle of the time-resolved spectral interferometry, reproduced from [7]. M: mirror; BS: beam splitter; S: sample; SL: slit, SP: spectrometer

while information on the imaginary part are provided in principle by optical transmission microscopy (OTM).

5.1.2 State of the art

Among the numerous pump-probe experiments developed since stable sources of light-pulses are commonly available [1], only a few are fully dedicated to in-situ observation of the refractive index change , i.e. directly in bulk dielectrics.

The technique of spectral interferometry [7] has the peculiarity of using two collinear probe-pulses separated by a fixed time delay. Between those two pulses, an off-axis pump pulse with a controllable delay with respect to the second probe pulse excites the transparent material of interest. The principle of this experiment is presented in Fig. 5.1. The time resolution is excellent and has been estimated around 120 fs, when pump and probe pulses have initial durations of about 80 fs. The two collinear probe pulses enter a spectrometer and interfere in the spectral domain. The power spectrum of the recorded interferogram carries an information directly related to the optical properties of the excited material. Although this method has proved its efficiency and offers an impressive temporal resolution, the spatial resolution of about 5 μm prevents it from being used in tight focusing conditions.

Sakakura and Terazima [8] implemented a collinear pump-probe setup based on the transient lens method (TrL) depicted in Fig. 5.2. The pump pulse excites the material in the focal volume. The excited area plays the role of a lens for the probe pulse. The probe pulse is focused at a distance d beyond the focal plane of the pump pulse. After propagation, the probe pulse is either spatially filtered through a pinhole to provide the TrL

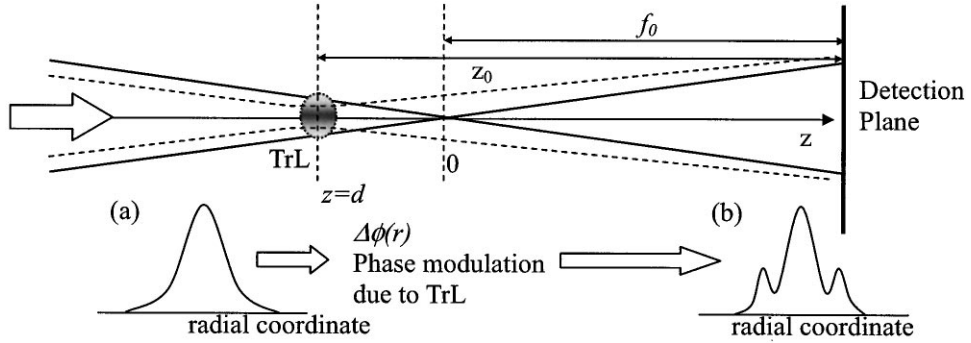[1]a remarkable "Smorgasbord of Pump-Probe Methods" can be found in [91]

Figure 5.2: Principle of the transient lens method, reproduced from [8]. The pump beam is focused at $z = d$ and the probe beam at $z = 0$

.

signal or analyzed by a CCD camera. Contrary to the previous method, the transient lens allows for analysis of small focal volumes. As a main drawback, this setup is not selective along the propagation axis as the recorded information is integrated over the whole focal region.

The pump-probe technique used by Sun et al. in [92] allows the monitoring of the real part and the imaginary part of the refractive index by performing interferential imaging and time-resolved shadowgraphs recording, respectively. Pump and probe pulses propagate in transverse directions. The main limitation of this experimental apparatus is the lack of spatial resolution in the interferential imaging mode.

Finally, Horn and coworkers [93, 94, 95] developed a time- and space-resolved microscopy setup employing absorption microscopy as well as Nomarski microscopy. The illumination source is a white-light continuum generated through a waterjet, allowing for spectral analysis as well. As a major drawback, a modification of the temporal response of the setupis likely to happen. Furthermore, as already mentioned in Ch. 3, Nomarski microscopy as a contrast enhancement technique may not be able to render all the subtleties of the refractive index map, as this technique is sensitive on refractive index gradients only.

We have developed a technique which allows time-resolved observations in optical transmission microscopy and phase contrast microscopy with a spatial resolution limited only by the characteristics of our microscope, and a temporal resolution better than 1 ps.
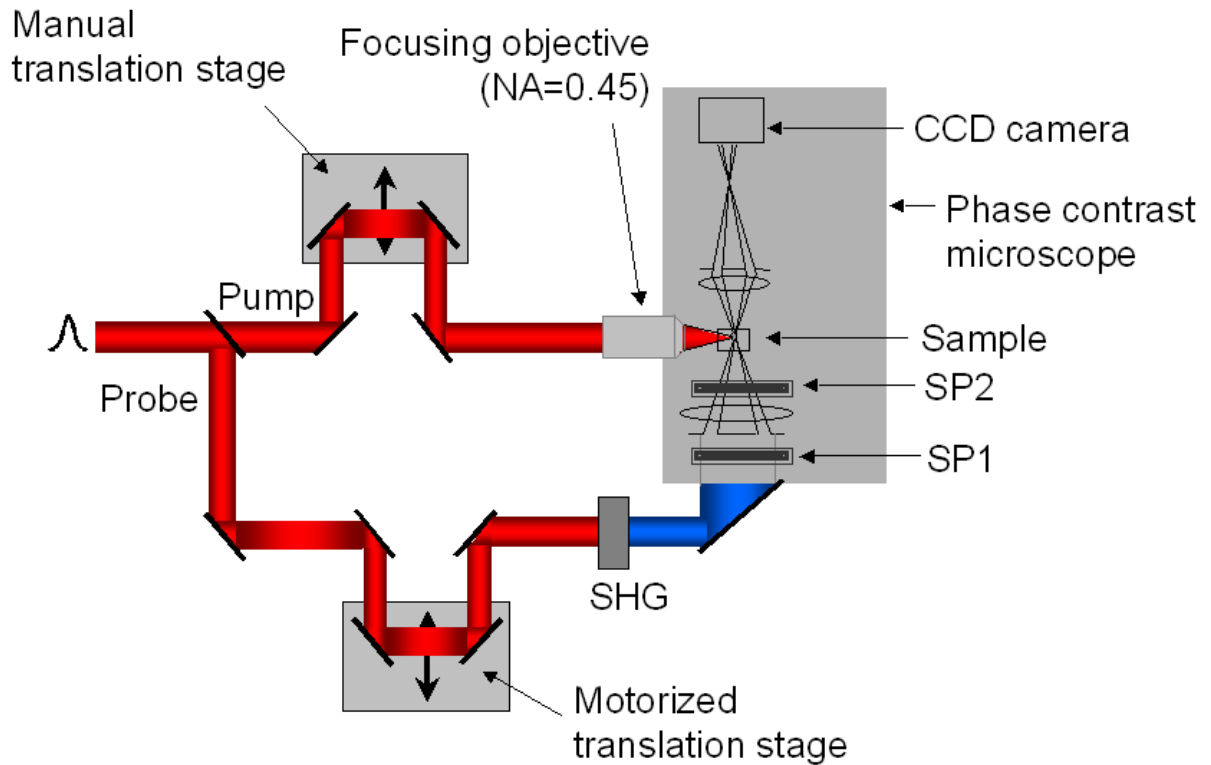
Figure 5.3: Principle of the pump-probe experiment. SHG: second harmonic generation, SP: scattering element.

5.2 Experimental realization

5.2.1 Pump-probe setup

A schematic of the setup used in the present work is shown in Fig. 5.3.

The laser sources used for the experiments are system II and IV as described in part 3.1.1. The path of the pump beam remains unchanged with respect to the previous chapter and only the illumination of the sample through the microscope is realized in a different way. A beam splitter distributes 10 % of the laser beam energy to the pump pulse and the remainder is used for illumination by the probe pulse. For that purpose, the light bulb initially located inside the housing of the microscope is removed, as well as the original collimation optics associated with it. The probe pulse is first frequency-doubled to 400 nm wavelength in a BBO crystal and then sent to illuminate the specimen via a long working distance condenser. The scenario illuminated by the probe pulse is then imaged by a phase contrast microscope objective on a CCD camera (iXon model from Andor Technology™). There is an obvious reason for probing at 400 nm. If the end of the pump pulse is scattered on a structure induced by the beginning of the pulse, the final image will be disturbed by

pump photons.

A second source of disturbances is the optical plasma emission from the highly excited region irradiated by the pump pulse which can be sensibly weakened by recording a narrow part of the spectrum only. For this purpose, an interferometric bandpass filter with a narrow bandwidth of 10 nm around 403 nm center wavelength is employed. As a major constraint, probing at a single wavelength generated via a second harmonic generation process has a non negligible cost in terms of pulse energy. For a good conversion, an efficiency of about 40 % is attained and an energy of about 95 μJ per pulse is left after conversion. The beam is then expanded by a telescope up to a diameter of about 25 mm and homogenized by a first scattering element (SP1) before entering the microscope. A second scattering plate (SP2) located between the collimator lens and the condenser provides a suitable source of illumination for the sample. Operating with scattering elements results in a dramatic increase of the noise via speckle generation which will alter the image quality on the detector camera.

A simple way to significantly reduce the deterioration of the signal-to-noise ratio is to average several speckle patterns. Practically, the second scattering plate is mounted on a rotating motor. In this way, random speckles patterns are generated and recorded. The sample is continuously scanned so that the laser irradiates each time a fresh spot. The final picture is a N-times accumulation of the same event but for different noisy backgrounds statistically canceling each other.

There is another reason for accumulating several pictures. Although an intensified camera is used, the amount of photons per pixel recorded in phase contrast microscopy is by far too weak to form a well-contrasted image.

5.2.2 Choice of a criterion for zero delay

A delicate aspect is the choice of a proper criterion for the synchronization between the pump and the probe. While in [7] the Kerr effect was conveniently used to know precisely when pump and probe overlap, we were not able to rely on this indicator. This point will be discussed later in this chapter. Sun and coworkers [92] could visualize the *propagation* of the pump pulse via the free carrier generation, this is not exploitable in our case because of the temporal and spatial resolution of our setup. As we usually use 40x to 80x magnifications, the field of view is about 150 μm wide in the most favorable case. Hence, the pump pulse takes roughly 500 fs to cross the entire field. As discussed in the next chapter, 500 fs is about the time resolution of our setup, rendering the pulse propagation tracking impossible.

However, a sharp rise in the absorption of the focal volume is visible immediately after free carrier generation. This was considered as an acceptable criterion to determine the

initial moment of excitation (zero delay). The pump-probe synchronization method is the following: : First, the pump pulse is significantly delayed with respect to the probe. The delay is then reduced until the onset of an absorbing zone starts to become visible. It is possible to equalize the pump and probe optical paths to within a $\pm 5\mu$m, providing a sufficiently good temporal accuracy for the zero delay of approximatively ± 35 fs.

5.2.3 Temporal resolution of the imaging system

Employing an imaging system like a phase contrast microscope is very interesting because of the potential advantages in terms of spatial resolution. Nevertheless, it has also important drawbacks. As pointed out by Bor [96] and emphasized in [11], single lenses constitute a non-negligible source of temporal broadening. An estimate of the total pulse streching can be obtained by evaluating the time interval between the arrival of an outer ray and the arrival of a ray on axis in the focal plane. The condenser of the phase microscope (cf. Fig. 3.12) consists of a single lens with a relatively short focal length f (f=16 mm in our case). The difference ΔT in time of arrival between an outer ray and an axial ray in the focal plane of the condenser is given by [11]

$$\Delta T = \frac{r^2}{2cf(n-1)}(-\lambda \frac{dn}{d\lambda}),$$ (5.1)

where r is the distance of the outer ray with respect to the optical axis, c is the speed of light in vacuum, n is the real part of the refractive index and depends on the wavelength λ considered. The condenser is made of a B270 Schott Glass with well known dispersion properties[2] and a refractive index of $n = 1.52$. For the value of r, we consider the most unfavorable case where $r = r_{condenser} = 10$ mm. The resulting broadening is ≈ 1.1 ps. It is important to note that for dispersion-corrected optical systems this effect is greatly reduced as shown in [96] for an achromatic doublet. Based on this observation, and although it is an arduous point to prove experimentally, the stretching experienced by the pump pulse when it reaches the focal plane of the focusing microscope objective is assumed to be negligible.

In phase contrast microscopy, the annular diaphragm placed in front of the condenser (cf. 3.12) greatly reduces the distance between outer and inner rays (r_{out} and r_{in}, respectively) from the optical axis. The corresponding amount of pulse broadening is obtained replacing r^2 by $r'^2 = r_{out}^2 - r_{in}^2$ in Eq. 5.1. Depending on the phase contrast objective used, the dimensions of the corresponding diaphragm vary. At our observation conditions, $r_{out} = 7.5$ mm, $r_{in} = 6.75$ mm and therefore $r'^2 = 10.7$ mm^2. Hence, the annular diaphragm reduces the pulse broadening by a factor of approximately 9, lowering the potential stretching down

---

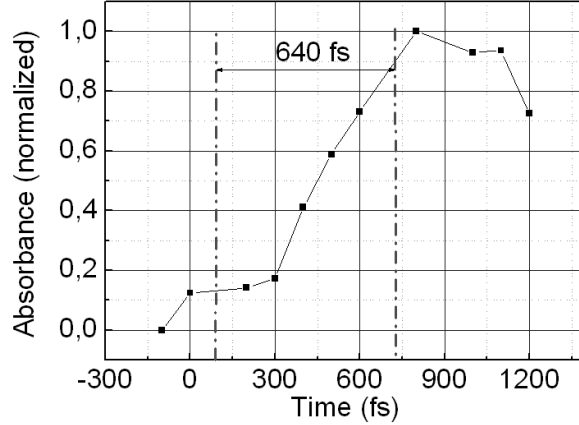[2]specifications on this type of glass are available at www.schott.com

Figure 5.4: Experimental estimate of the temporal resolution of the pump-probe setup.

to the order of the original pulse duration. In conclusion, if the pulse broadening due to the condenser is not expected to be significant in the phase contrast mode, the consequences might be substantial in the optical transmission mode (OTM).

We propose an experimental estimate of the pulse broadening in the transmission mode based on the following principle. The free-carrier generation is supposed to take place within the laser pulse duration only. Hence, the absorption due to the electron gas presumably rises within about 100 fs. The assumption that the probe beam absorption is exclusively due to the free carriers is probably only valid in the regions where the material is excited below the damage threshold. If the electron-hole plasma is too dense, other reasons like the formation of scattering structures or partial reflexion of the incoming light on the mirror-like structure formed by the electron-hole plasma can be responsible for a low transmission coefficient. For this reason, the dynamic evolution of the ratio of transmitted intensity on axis is evaluated well before the geometric focus of the laser pulse. In this region, although a strong absorption shows up, no permanent traces of damage could be detected. The results are presented in Fig. 5.4. The rise time from 10 % to 90% of the absorption is arbitrarily taken as the time for absorption rise. Assuming the free carrier generation to follow the laser intensity, the experimental result shows that free carrier generation is actually visible for about 640 fs, a half compared to the above estimate of the time resolution. This discrepancy is most likely due to the difficulty to assign an accurate value for r in Eq. 5.1, as in normal transmission microscopy the back surface of the condenser is not totally illuminated because of the different diaphragms on the optical path.

We attempted to improve the time resolution by pre-chirping the pulse, in order to anticipate the effect of group velocity dispersion. No significant benefits in terms of temporal resolution could be obtained. This result is not very surprising considering the relatively

narrow spectrum of system II (about 10 nm width).

In the last chapter, laser matter interaction has been presented from two extreme temporal points of view. The results of simulations provided indications about the very first moments of the energy coupling inside the bulk during illumination and the static phase contrast pictures shown the permanent consequences of the laser action on the refractive index of the material.

This chapter aims at filling the missing temporal gap by probing the dynamic reaction of the irradiated target to the laser irradiation on the timescale of energy relaxation (ps-ns). By monitoring the complex refractive index as a function of time, relevant informations about the transient properties of the material can be gathered, as well as an identification of the mechanisms involved in changing the local optical properties. The basic idea of this series of experiments is to benefit from the spatial resolution offered by a microscope and from the temporal characteristics of the femtosecond pulse.

The chapter is organized as follows. The first section deals with the general principles of pump-probe experiments and includes a survey of pump-probe experiments already developed for in situ monitoring of laser interaction with bulk transparent materials. The second section focuses on the implementation of our pump-probe setup. The limits and the performance of our apparatus are evaluated and commented. The rest of the chapter contains a presentation and a discussion of the experimental results. Section 5.3 shows experimental results in the case of a high laser pulse energy for BK7 and a-SiO$_2$, the following section deals with laser pulse energies close to the modification threshold and finally, an application of the time-resolved OTM setup is proposed in the last section, where the lifetime of the free carriers is evaluated for BK7 and for another optical glass (IOG-10).

5.3   Time-resolved phase contrast pictures at high input energies

In this section, we aim at following the dynamics of the refractive index change when the input energy is above 15 μJ, that is to say in the strong interaction regime defined in Sec. 4.1.1 for fused silica. The discussion focuses on high input energies because the size of the structural changes is expected to facilitate the observation. The interaction in the case of low laser energy will be treated later in this chapter.
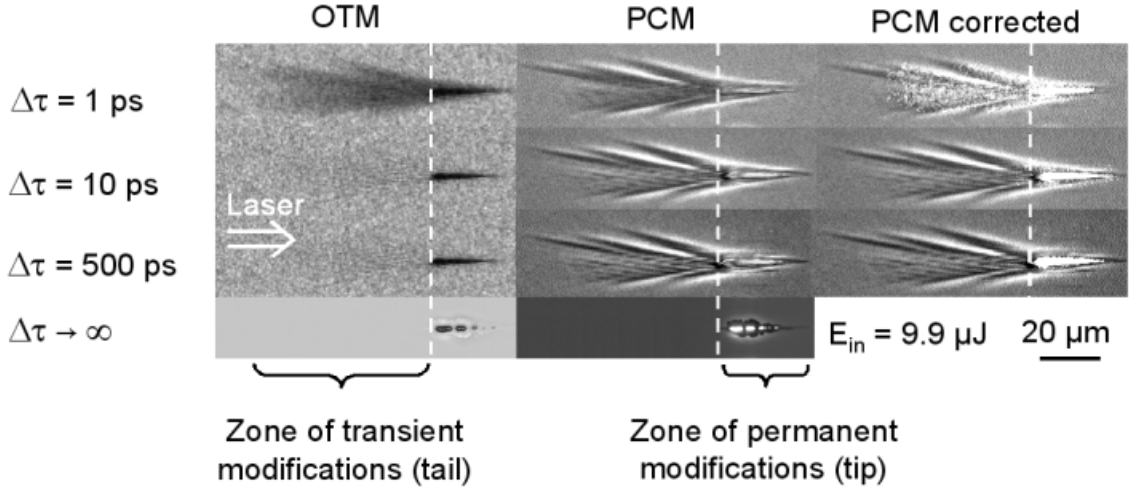
Figure 5.5: Time-resolved observations in optical transmission microscopy (OTM) and phase contrast microscopy (PCM) in fused silica for pump-probe delays of 1 ps, 10 ps and 500 ps. For the comparison, PCM and OTM pictures of the permanent imprint are shown. Phase contrast microscopy observations corrected from absorption (PCM corrected) are also presented for the time-resolved pictures. The laser pulse energy is 9.9 μJ. The regions permanently modified are indicated with dashed lines.

5.3.1 Experimental conditions and selected results

The investigations have been carried out with system II. The laser pulse energy is 9.9 μJ, close to the modification threshold detectable with the PCM setup. In order to obtain a satisfying signal-to-noise ratio, 25 pictures for each time point were accumulated in the PCM mode, and 12 pictures were accumulated in the OTM mode. Results are presented in Fig. 5.5 for a-SiO$_2$ and in Fig. 5.6 for BK7, respectively. Time-resolved OTM pictures are presented in the left column, whereas time-resolved PCM pictures appear in the middle column. Additionally, we also propose time-resolved PCM pictures corrected from absorption (see Sec. 3.36). Although those time-resolved measurements have been carried out at numerous time delays $\Delta\tau$ between the pump pulse and the probe pulse covering the range $0 < \Delta\tau < 500$ ps, we decided to restrict the presentation of the experimental results to three values of $\Delta\tau$, sufficient to support the following discussion.
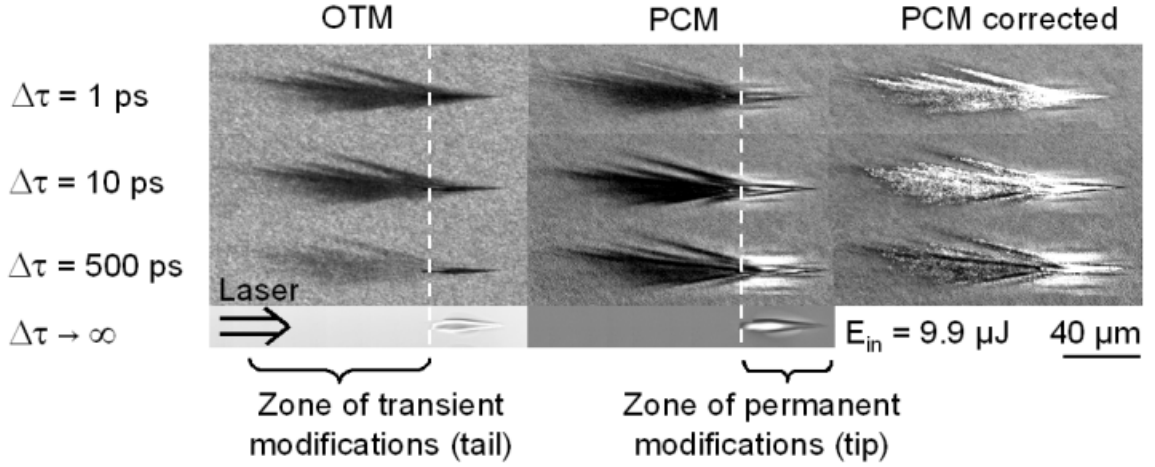
Figure 5.6: Time-resolved observations in optical transmission microscopy (OTM) and phase contrast microscopy (PCM) in BK7 for pump-probe delays of 1 ps, 10 ps and 500 ps. Otherwise as Fig. 5.5.

5.3.2   Discussion

Comparison with PCM observations in white light

Surprisingly, Fig. 5.5 and Fig. 5.6 show that at the given pulse energy, the axial extent of the region affected transiently is three times larger than the axial extent in the permanent regime. This holds for both materials studied. Based on this observation, we divide the interaction zone in two parts, the "tail" and the "tip". The tail corresponds to the part of the material experiencing transient modifications only and the tip refers to the region of permanent modification.

Kerr effect

We did not find any experimental evidence for the Kerr effect at short timescales, when both pump and probe pulses overlap in time at the same location into the sample (no pictures shown here). At first sight, this seems to be in contradiction with respect to earlier work (see for instance [44]) where a nonlinear coupling between the pump and the probe pulses results in a transient modulation of the refractive index (see Sec. 2.2.1 for further explanations about the Kerr effect).

We believe that this contribution could not be detected for two reasons. At first, the pump-probe setup configuration is not favorable to the observation of the Kerr effect. The pump and and probe beams are perpendicular to each other, which minimizes the overlapping length between pump and probe pulses. Therefore, the resulting phase shift experienced by
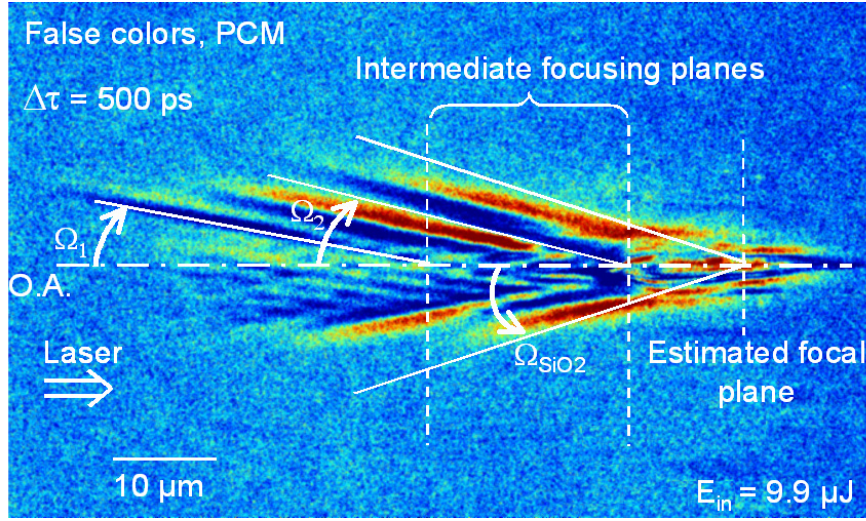
Figure 5.7: Time-resolved PCM picture in a-SiO$_2$ (false colors) 500 ps after excitation. The location of the optical axis (O.A.), the location of the estimated focal plane and the half-angle of the focusing cone Ω_{SiO2} are indicated. The laser pulse energy is of 9.9 μJ.

the probe beam is also greatly minimized. Moreover, a somehow analogous effect takes place in the time domain. From the discussion on the time resolution presented in Sec. 5.2.3, it appears that the probe pulse has a significantly longer duration than the pump. The probe pulse duration determining the effective exposure time on the CCD matrix, the contribution of the Kerr effect to the final picture is thus integrated over a time window much longer than its existence. Both effects prevent an observation of the Kerr effect.

Structure of the tail

According to Eq. 3.12, the laser energy is confined in a cone of half angle Ω, depending exclusively on the numerical aperture of the focusing objective NA and on the refractive index of the propagating medium n via

$$\Omega = \arcsin\left(\frac{NA}{n}\right). \tag{5.2}$$

At a wavelength of 800 nm, we find $\Omega_{SiO2} = 18°$ and $\Phi_{BK7} = 17° \ 25'$ for a-SiO$_2$ and BK7, respectively. The focusing cone is drawn as solid white lines in Fig. 5.7 for fused silica. This figure corresponds to a PCM observation in a-SiO$_2$ with $\Delta\tau =$500 ps delay but for the purpose of the discussion, the colormap is artificially modified and the contrast is uniformly enhanced in order to highlight relevant features.

Figure 5.7 shows a characteristic interference pattern in the region excited at intensities below the permanent modification threshold. This region is indeed well restricted to the

geometric focusing cone. Interestingly, further investigations reveal that lines of isointensity, appearing with a uniform color, propagate with different angles (two angles Ω_1 and Ω_2 have been drawn) and intercept the optical axis in distinct intermediary focusing planes. In the following discussion, we attempt to propose a plausible explanation for this phenomenon.

The overall envelope of the modified region strongly resembles the plasma shapes reported by Vogel et al. in presence of spherical aberrations [97]. A hypothetical role of spherical aberrations would not be in contradiction with the simulations carried out earlier in Ch. 3.2.2, as we are aware that our focusing conditions experimentally minimize the spherical aberrations without fully canceling them.

A careful examination of Fig. 5.7 confirms this hypothesis. Isointensity lines characterized by an angle Ω_1 intercept the optical axis earlier than isointensity lines characterized by an angle Ω_2. Direct estimations from the picture give $\Omega_1 = 10° \ 30'$ and $\Omega_2 = 14°$, meaning that inner rays of the focusing cone are focused stronger than outer rays. This corresponds well to the situation depicted in Fig. 3.6, where the paraxial focal plane is located closer to the air-glass interface than the focal plane associated to the peripheral rays.

Additionally, a competition between the residual spherical aberrations and self-focusing (SF) takes place. At early times during the pulse propagation, i.e. when the laser energy is moderate, spherical aberrations govern the energy deposition. When the laser energy is higher, SF reinforces the effect of spherical aberrations. Since the intensity of the pulse is higher at small radial coordinates, the SF lens is by far more efficient in the central part of the beam and results in a premature collapse of the paraxial rays. Moreover, laser pulse defocusing takes place when propagating through the free carrier gas generated earlier by the leading edge of the pulse. In this way, additional energy can possibly be deposited in the region of the tip by a filamentation process, where SF and defocusing on the induced electron plasma balance and drive away the laser pulse energy.

Altogether, the respective contributions of spherical aberrations, electron defocusing and SF result in different propagation angles depending on the beam intensity in space and time. As a consequence, some of the rays cross and interfere, resulting in the interference pattern visible in Fig. 5.7.

In the case of BK7, such a modulated interference pattern could not be observed, but instead, the modified zone seems to be uniformly excited. This different behavior is attributed to the different bandgap energies of fused silica (7.5 to 9 eV) and BK7 (about 4.1 eV). The interference pattern does not have a maximal contrast, and in the zones of destructive interferences the residual energy may still exceed the modification threshold in BK7, smearing out the small structures visible in the case of a-SiO$_2$.

At this point, it is very tempting to assign the presence of the small dots visible in Fig. 4.4

to the interplay of nonlinear propagation and spherical aberrations as well, rather than to a partial reflexion of the incoming energy as firstly suggested in Sec. 4.1.1. Additional work in this direction is being carried out at the present time and will be presented in a future publication.

Influence of the electron gas on the transient refractive index

The contribution of the free carriers to the refractive index has been previously treated within the frame of the Drude model in Sec. 2.3.2. When free carriers are generated, a decrease of the real part of the refractive index and an increase of the absorption are expected.

On the OTM pictures presented in Fig. 5.6 and Fig. 5.5, the interaction region is characterized by the onset of a pronounced absorption. This strong absorption is attributed to an inverse bremsstrahlung process between the laser generated free carriers and the photons from the probe pulse. The PCM pictures are substantially affected by this absorption and exhibit a misleading black region in the tail.

Subtracting the influence of the absorption (see Eq. 3.36) reveals the influence of the free carriers on the real part of the refractive index, and the focusing cone appears brighter than the background, as predicted by the Drude model. The free carrier density gradually decreases on a picosecond timescale.

In fused silica and BK7, the dynamics is very different. Whereas lifetimes of about 150 fs have been reported for fused silica ([7, 92]), a comparison between the time-resolved OTM pictures presented in Fig. 5.6 and 5.5 shows that the relaxation time in BK7 is considerably longer. We propose an estimation of this relaxation time at a later point in this chapter.

Energy relaxation into the bulk

As the influence of the free carriers on the refractive index gradually diminishes with time, the imprint of the excited zone remains visible in fused silica. This zone, easily discernible in Fig. 5.5, corresponds essentially to an increase of the refractive index and is detectable up to 500 ps. We believe that this feature corresponds to the optical signature of the relaxation of the energy stored in the free electron gas. The energy can be relaxed in two ways, either via point defect creation, or via heat transfer. According to Toyoda and Yabe [98], the refractive index of fused silica increases with temperature, at least up to 400°C and in Ch. 2.5.2, we stated that point defects with proper energy levels in the bandgap also contribute to an increase of the refractive index. Nonetheless, we can speculate that we mostly see here thermal effects, because the zone stays astonishingly unchanged, from 10 to 500 ps after excitation in a-SiO$_2$, whereas a zone with a high concentration of transient point defects

would be expected to evolve over such a time window. In order to draw a more indisputable conclusion, repeating the same experiment at different probing wavelengths would provide precious arguments.

Finally, we draw attention on a further intriguing point. In fused silica only, well contrasted white lines appear in the periphery of the excitation envelope (see Fig. 5.5). At present, we could not find a satisfying explanation of their origin.

5.3.3 Conclusion

In conclusion, several points are noteworthy. At high laser energies, the excited region largely exceeds the zone of permanent modification, and a transient feature (the tail) appears. The imprint visible in PCM after relaxation is limited to the tip of the focusing cone. Unfortunately, this region is difficult to study in the regime of high energy irradiation, probably because several parasite phenomena such as plasma emission screen the relevant information. Therefore, we report a study with a laser energy slightly above the modification threshold in the next chapter. The study of the tail gives insight into energy deposition mechanisms, and illustrates the importance of self-focusing. The global plasma shape is the result of an interplay between nonlinear propagation phenomena and possibly residual spherical aberrations. Additionally, time-resolved OTM pictures show the different energy relaxation rates of the free carriers in BK7 and fused silica. This is exploited at a later point in this chapter, when we report a quantitative study of the free carrier lifetime in BK7.

5.4 Time-resolved phase contrast pictures at low input energies

In the previous section, the study focused exclusively on the phenomena in regions of transient modification. Information in the zone corresponding to the region of permanent modification could not be exploited, in particular because of optical plasma emission. We now describe a study at a laser energy slightly above the modification threshold. At first, a low input energy should appreciably reduce the amount of parasitic light from the electron-hole plasma created in the focal volume. Secondly, those conditions are closer to the energy range encountered when usually processing dielectrics at tight focusing conditions, and can potentially provide useful informations for the optimization of laser processing of transparent materials.
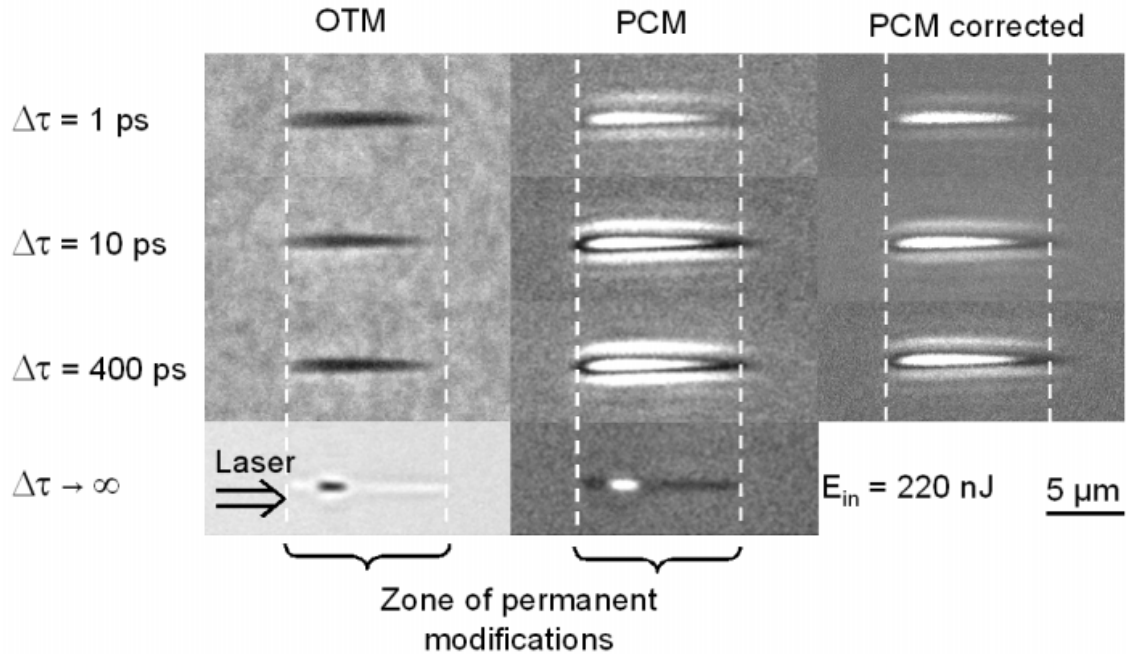
Figure 5.8: Time-resolved observations in optical transmission microscopy (OTM) and phase contrast microscopy (PCM) in fused silica for pump-probe pulses delays of 1 ps, 10 ps and 400 ps. For comparison, PCM and OTM pictures of the permanent laser-induced traces are shown. Phase contrast microscopy observations corrected from absorption (PCM corrected) are also presented for the time-resolved pictures. The laser pulse energy is 220 nJ. The regions permanently modified are indicated with dashed lines.

5.4.1 Experimental conditions and selected results

This series of investigations has been carried out with system II. The laser energy is of 220 nJ, close to the modification threshold detectable with the PCM apparatus. 100 pictures were accumulated for each delay time to obtain a good signal to noise ratio in PCM, and 50 pictures were accumulated in OTM.

Some selected results are presented in Fig. 5.8 for time delays between the pump and the probe pulses ($\Delta\tau$) of 1 ps, 10 ps and 400 ps. For comparison, a permanent trace is also shown. In the left column, time-resolved OTM pictures are presented, time-resolved PCM pictures appear in the central column, and time-resolved PCM pictures corrected from absorption (see Sec. 3.36) are also shown in the right column.

The lack of similarity between the time-resolved pictures and the appearance of the permanent imprint suggests that energy relaxation phenomena take place on the nanosecond timescale. Therefore, the capabilities of the setup was extended to time delays of 4.5 ns, 7 ns and 9.5 ns. The corresponding pictures as well as an additional picture at $\Delta\tau = 800$ ps
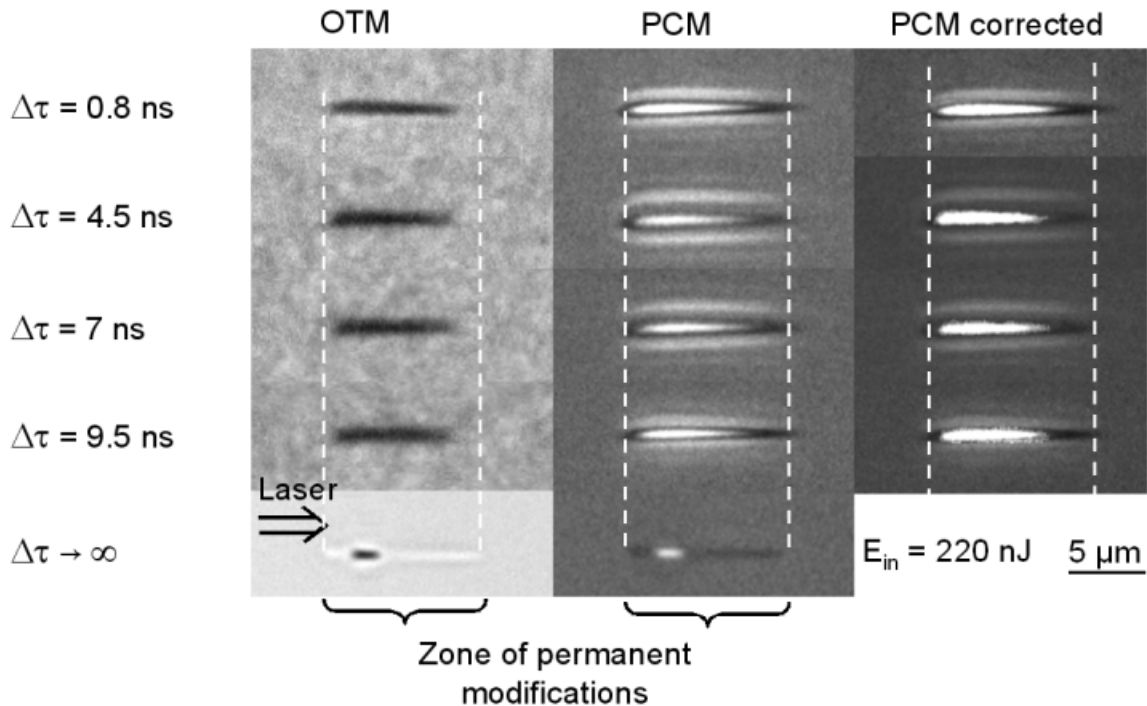
Figure 5.9: Time-resolved observations in optical transmission microscopy (OTM) and phase contrast microscopy (PCM) in fused silica for pump-probe delays of 0.8 ns, 4.5 ns and 9.5 ns. Otherwise, as Fig. 5.8.

are shown in Fig. 5.9.

5.4.2 Discussion

Comparison of transient pictures with PCM observations in white light

Contrary to the high laser energy regime studied in the last section, the zone where the energy is coupled to the material is now confined to the vicinity of the permanently modified region, and no feature such as the tail previously described can be detected anymore. The longitudinal dimensions of the transiently affected region and of the permanent imprint are very similar, as axial extensions of 10.5 μm and 9.5 μm respectively, are estimated from Fig. 5.8.

The radial extent is more delicate to evaluate. From the non-corrected time-resolved PCM pictures, a large white halo is visible at a distance of approximately 1.3 μm from the optical axis, invisible on the permanent PCM picture. At first, we tried to evaluate the intensity of this halo in an infinitely thin layer corresponding to the observation plane. In
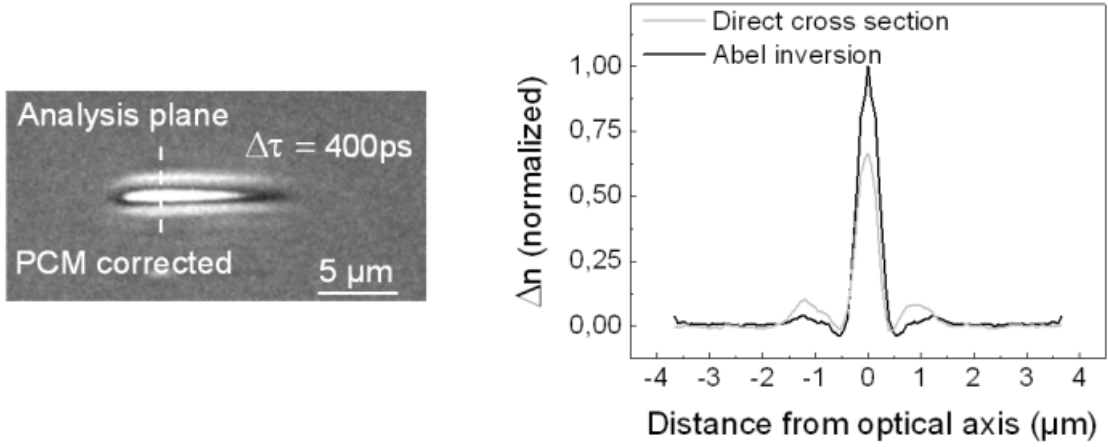
Figure 5.10: Estimate of the importance of the halo visible in phase contrast microscopy (PCM) observations. On the left, a time-resolved PCM observation corresponding to a laser energy of 220 nJ and a pump-probe pulse delay of 400 ps is presented. On the right hand side, we show the result of the Abel inversion in the analysis plane indicated by the dashed line. For comparison, the original grey-level profile in the analysis plane is plotted in the same graph.

this purpose, an Abel inversion was performed [3], to cancel the misleading influence of the cylindrical geometry on the final picture. The results of an Abel inversion at an arbitrary on-axis location is shown in Fig. 5.10. The example presented is based on a PCM picture taken at $\Delta\tau = 400$ ps, as it corresponds to a maximum intensity of this halo.

The Abel inversion unambiguously minimizes the amplitude of this phenomenon. Furthermore, we noticed that the brightness of the halo follows the amplitude of the the refractive index change in the central region. Hence, we believe that this feature arises from a PCM artifact probably due to probe light deflection [99] on the laser-excited region. Finally, the effective radial extent of the modified zone is limited to the black shell surrounding the electron plasma. It is estimated at a transient value of 1 μm. The transversal dimension of the permanent filament is slightly smaller, around 0.7 μm.

On axis refractive index profile

We now carry out an analysis of the axial profile of the refractive index distribution in the transient regime. To this extent, an axial cross section (ACS) was performed on some transient pictures along the optical axis (see Fig 5.11).

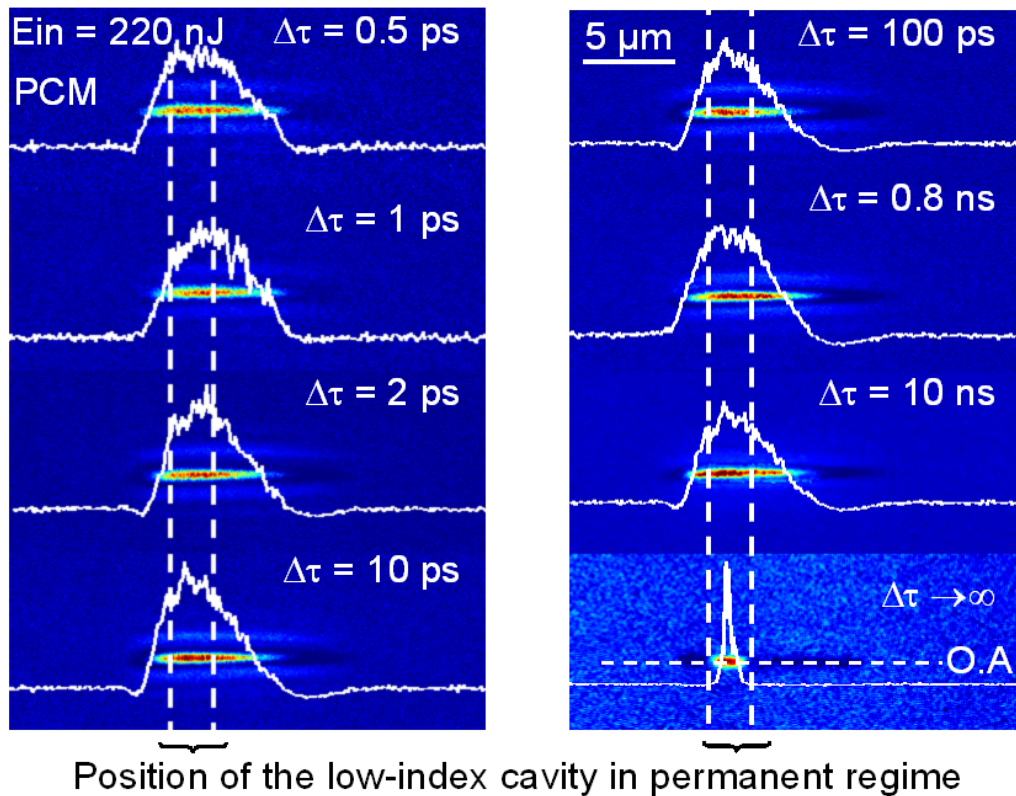[3]The calculations were performed with the software Spotlight-16, available at http://microgravity.grc.nasa.gov

Figure 5.11: Time-resolved PCM observations corresponding to a laser pulse energy of 220 nJ for different pump-probe delays $(\Delta\tau)$ in bulk a-SiO$_2$. The colormap and the contrast were adjusted to enhance the intensity variations in the central region of energy deposition. The corresponding axial cross sections along the optical axis (O.A.) are overlapped with the original time-resolved PCM images. The region between the dashed bars corresponds to the zone where a low index cavity (void) remains visible in permanent regime $(\Delta\tau \to \infty)$.

In Fig. 5.8 and 5.9, the center of the focusing region looks uniformly white on the PCM images. This is because the contrast was enhanced in order to make visible all the characteristic features of the laser affected volume, in particular the periphery of the central region.

We now perform a study of the exact on-axis intensity recorded experimentally. Comparing the transient axial cross sections (transient ACS) with the ACS obtained from the permanent trace ($\Delta\tau \to \infty$) reveals that *the low-index cavity (void) visible in permanent regime exactly corresponds to a peak of the transient ACS for $\Delta\tau \geq 2$ ps.* This is shown in Fig. 5.11 where the region corresponding to the low-index cavity is located between the dashed bars. It is not possible to establish such a correspondence at time delays smaller than 2 ps, suggesting that the onset of a peak on the transient ACS, and therefore the formation of the void is linked to a thermal mechanism [82].

At first sight, assigning a temperature elevation to a white zone in PCM (red on the colormap used in Fig.5.11), seems to be in contradiction with the results of Toyoda et al. [98], expecting an increase of refractive index Δn with the temperature, at least up to 400 °C in fused silica. Speculatively, the temperature of the material may be well beyond, in a regime where the local density (and therefore the refractive index of hot fused silica) decreases. This behavior is well known for silica glasses where the volume-temperature curve shows a local minimum at about $T' = 1500$°C [100]. This tends to disagree with our previous simulation results, where a maximal temperature of about 700°C is expected for a laser energy of 1 μJ (see Sec. 4.1.1). However, the results reported in [98, 100] are obtained on samples heated at ambient pressure. The consequences of bulk confinement on T' have not been clarified to our knowledge, leaving open the possibility of a transition temperature shifted to lower values. In conclusion, the refractive index decrease observed in PCM could be a result of strong heating.

For simplicity, we assume that in the region of the void, the refractive index change is mostly driven by thermal mechanisms and that the refractive index change is essentially due to a local material expansion $\Delta\varrho/\varrho$. Under such conditions, the relative refractive index change $\Delta n/n$ is directly proportional to the volume change $\Delta V/V$ [83]. In this scenario, the void arises from a thermomechanical effect, where the final density of the material depends on the temperature map immediately after excitation. Fig. 5.11 shows that the void formation has a sharp intensity threshold in PCM, meaning that above a certain deposited energy density, the material is driven into a low density state while below, the material cools down in a higher density state than the pristine bulk. More information needed to confirm this hypothesis is provided in the next paragraph, where the dynamics of void formation is studied.
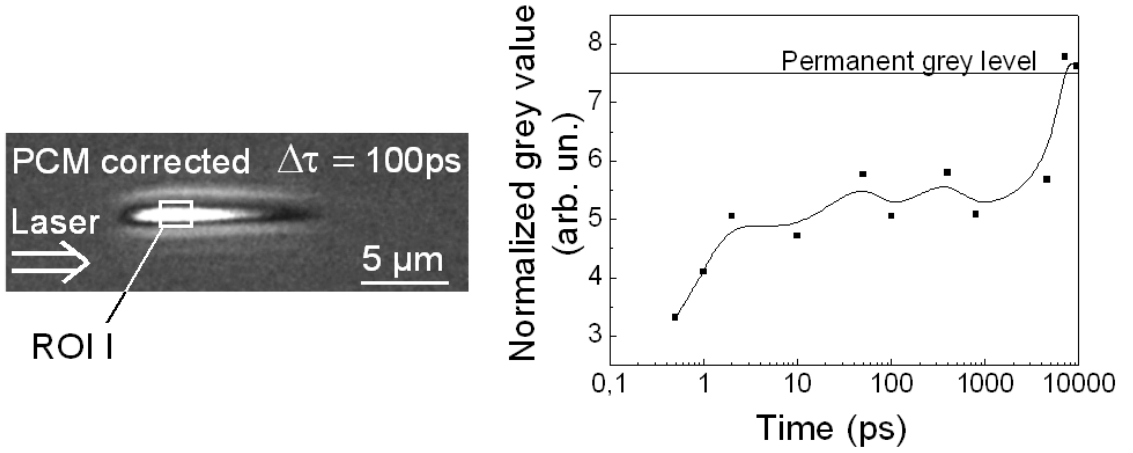
Figure 5.12: On the left, a time-resolved PCM observation corresponding to a laser energy of 220 nJ and a pump-probe delay of 100 ps is presented. On the right, the evolution of the region of interest (ROI I) is plot versus time. The value of ROI I in permanent regime is indicated on the graph.

Dynamics of void formation

A particular region of interest (ROI I) corresponding to the spatial extent of the void visible in permanent regime is shown on the PCM transient pictures. The average gray level of ROI I is divided by the mean value of the background. The value of the ratio obtained for each pump-probe delay is plotted in Fig. 5.12, where the horizontal line corresponds to the final gray value of the region being studied. Moreover, an interpolation based on splines is proposed to guide the eye.

The region resulting in a void evolves in three steps. The first phenomenon, from 0 to 2 ps, leads to a moderated decrease of refractive index. Because of the timescale, this first step could well show the gradual energy transfer from the free carriers to the lattice, in good agreement with the estimations of Juodkazis et al. (see for instance [81, 82]).

When the heat is transferred to the lattice, hydrodynamic motion commences. From 2ps to 4.5 ns, Δn slightly increases and oscillates around a value close to its value after heat transfer. Between 4.5 and 7 ns, a brutal event takes place with a sharp impact on Δn. The material is then close to its final state.

The oscillatory behavior of the optical properties, the timescales involved and the a priori relatively low temperature (well below the softening point according to the simulation results) in the focal volume plead for the onset of thermoelastic phenomena, in agreement with the observations of Sakakura et al. [8]. In this scenario, the material experiences a mechanical constraint due to the temperature elevation. This thermomechanical effect
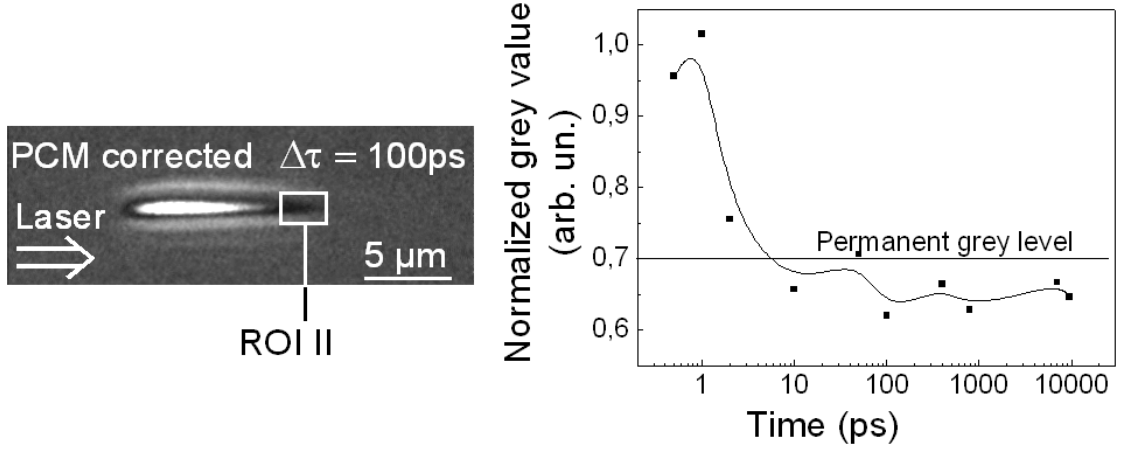
Figure 5.13: On the left, a time-resolved PCM observation corresponding to a laser energy of 220 nJ and a pump-probe delay of 100 ps is presented. On the right, the evolution of the region of interest (ROI II) is plot versus time. The value of ROI II in permanent regime is indicated on the graph.

results in a deformation beyond the elastic limit on the nanosecond scale and translates into the generation of a permanent void. We will now describe the same type of study in the filamentary region.

Evolution of the refractive index at the extremity of the filament

The same method as before is employed for analyzing the extremity of the filament, and a region of interest (ROI II) is determined as indicated in Fig. 5.13.

Between 10 ps and 4.5 ns, the same oscillatory behavior as before is observed, but this time, it lasts until at least 9.5 ns after laser excitation. At this point, the material has still not reached its permanent state. Interestingly, we could not detect any absorption within ROI II. One reason can be that the free electron density is not high enough to be detected, and is screened by the residual speckles. This low energy density region results in moderate bulk heating and translates into a local increase of the material density upon cooling. This purely thermal scenario is in good agreement with the timescales observed. Additionally, the role of defects can not be excluded, and would also be consistent with the low transient absorption coefficient observed in ROI II. To this extent, further experiments including a spectral study are in preparation.
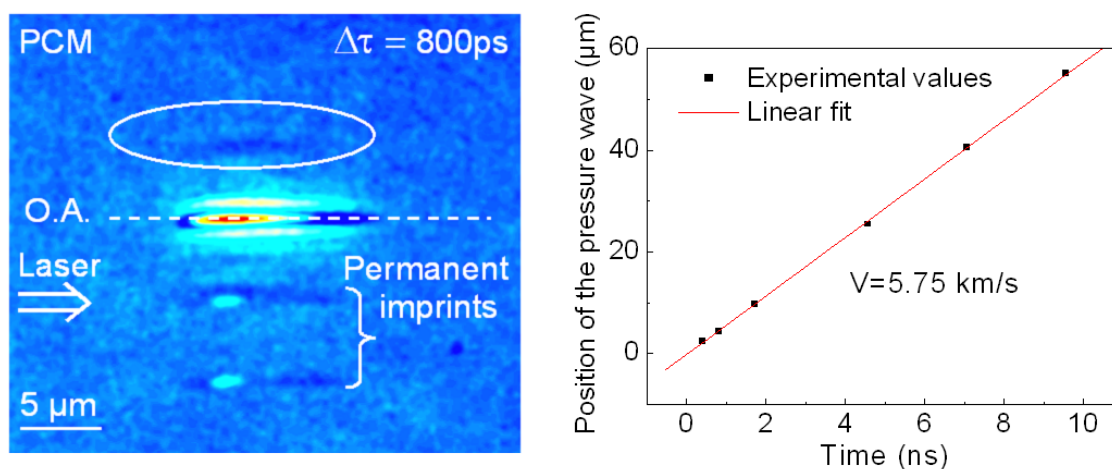
Figure 5.14: On the left hand side, a time-resolved PCM observation (false colors) corresponding to a laser pulse energy of 220 nJ and a pump-probe pulse delay of 800 ps is presented. The region where the pressure wave is visible is indicated. On the right hand side, the position of the pressure wave with respect to the optical axis (O.A.) is plotted versus time.

Pressure wave generation

After the free carriers receive kinetic energy from the pump laser pulse by inverse bremsstrahlung, an energy transfer to the lattice commences via phonon generation. In fused silica, the short lifetime of the free carriers (observed in the last section) suggests that this phenomenon is rather fast. As a result, a mechanical wave, emerges from the center of the interaction region. Although the consequences of this pressure wave on the refractive index are expected to be very subtle, we have been able to detect a local refractive index change propagating into the pristine bulk. In Fig. 5.14 we changed the usual colormap of a PCM picture and enhanced the contrast in order to make this local perturbation visible. The position of the maximum of this wave was tracked in time and plotted in Fig. 5.14. This wave propagates with a velocity of 5.75 km/s, close to the velocity of a sound wave (5.57 km/s in fused silica according to [101]).

5.4.3   Conclusion

As a summary, the following point should be highlighted. We propose that the refractive index change is mostly driven by a thermomechanical phenomenon. Below a certain initial temperature, the material cools down in a higher density state, and above this temperature, the material experiences a thermoplastic transformation resulting in the formation of a void.
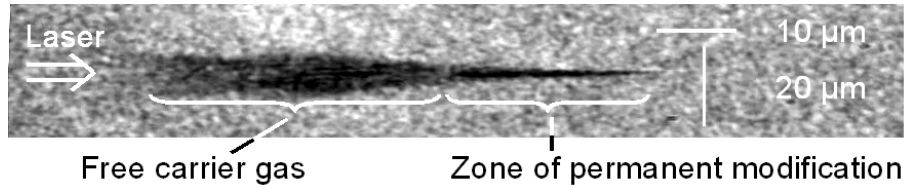
Figure 5.15: Example of transient absorption picture in Bk7.

5.5 Free carrier lifetime in BK7 and IOG-10

In this section, we present a useful application of our time-resolved OTM setup. While the lifetime of free carriers in fused silica is known for a decade [7], it is difficult to find this information for other glasses. This material property may be of interest in the context of controlling the laser writing of optical structures. Therefore, we evaluate the lifetime of the free carriers in BK7. Potentially, this technique can be employed to characterize any transparent material. As an illustration, we also investigate IOG-10, a glass commonly used in optical applications. Some time-resolved OTM images have already been shown in the previous section. Therefore, the discussion will not focus on the description of individual pictures again. Instead, we now put the emphasis on the description of the transient absorption and show how to use this information to get a quantitative estimate of the free carrier lifetime.

5.5.1 Experimental conditions and presentation of the results

A typical picture of the transient absorption is shown in Fig. 5.15. This picture has been taken with a conventional camera, manufactured by Jai, model CV-A1. The laser source we used is system IV. As briefly mentioned in the previous section, the absorption zone exceeds by far the dimensions of the damaged area as shown in Fig. 5.15 where the length of a permanent trace is indicated.

Qualitatively, when different delays between pump and probe are explored, the general behavior of absorption is depicted in Fig. 5.16. At first, the absorption slowly increases until about 0.6 ps. This gradual increase corresponds to the time-resolution of our setup, as explained in the previous section. The schematic absorption curve then shows a negative slope. In regions where the density of carriers is presumably low, that is to say where the material is excited but not modified in a permanent way, Fresnel reflection from the electron plasma is negligible. Therefore, in those regions, the absorption decay is associated to the progressive recombination of the free carriers.
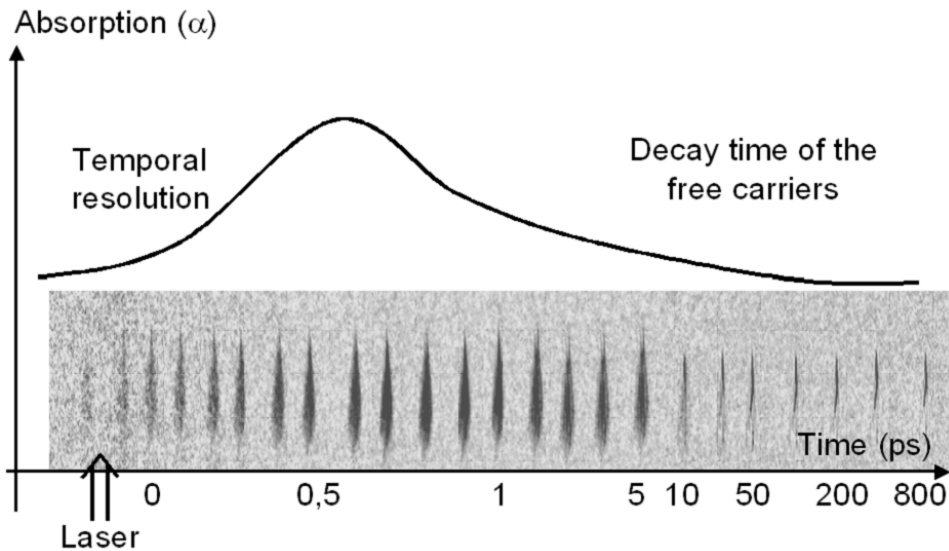
Figure 5.16: Overview of the free carrier absorption versus time.

5.5.2   Quantitative estimate of the free carrier lifetime in BK7 and IOG-10

Quantitative measurements have been performed for Bk7 and IOG-10, based on the analysis of transient absorption pictures. The procedure followed to exploit the experimental results is detailed in appendix.

The time resolution of the setup prohibits quantitative studies in a-SiO$_2$ as the dynamics are extremely fast in this material (decay times of 150 fs have been reported for the free carrier absorption, see [7, 92]). Results for BK7 are presented in Fig. 5.17. The transmission picture proposed has been taken 1 ps after excitation. In the zone carrying a permanent signature of the laser action, between the bars, the reliability of the results is disputable and will be not discussed. At first, the small transverse dimension of the absorbing cone is troublesome for determining the thickness of the electron gas (L) with reasonable certainty. This lack of precision results in spikes as can be seen from Fig. 5.17 on pixels 521 and 522. The same difficulty holds far from the focal region. The absorption cone divides into filaments and it is difficult to assign a definitive value for L. Then, the probe beam attenuation may not be exclusively due to free carrier absorption but also to deflection, reflexion and scattering on the laser affected region. We mention that for those reasons, the absolute real electronic density may be overestimated. In the region of transient modifications, the mean density of free carriers has an average value of 5.8×10^{19} cm^{-3}, almost one order of magnitude less than in the focal region. Remarkably, the electron gas seems to have a constant density over a length of about 30 μm.
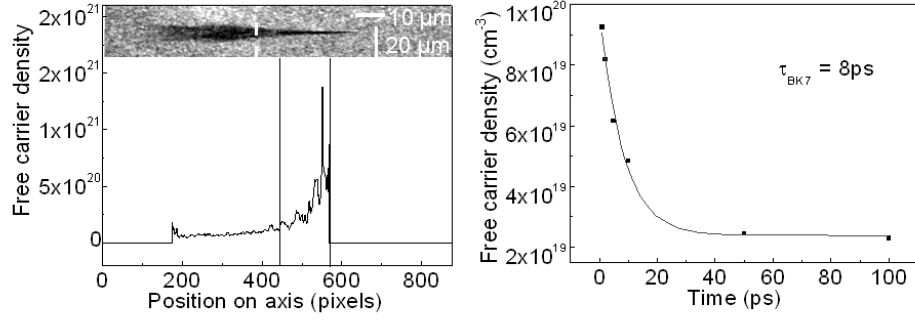
Figure 5.17: Free carrier density estimate 1 ps after excitation (left) in BK7. The region between the solid lines corresponds to the region of permanent modification. On the right, the free carrier density in the plane indicated by the dashed line is plotted for different values of $\Delta\tau$. The estimate of the free carrier decay rate (τ_{BK7}) is deduced from a fit of the experimental points by a first order exponential decay.
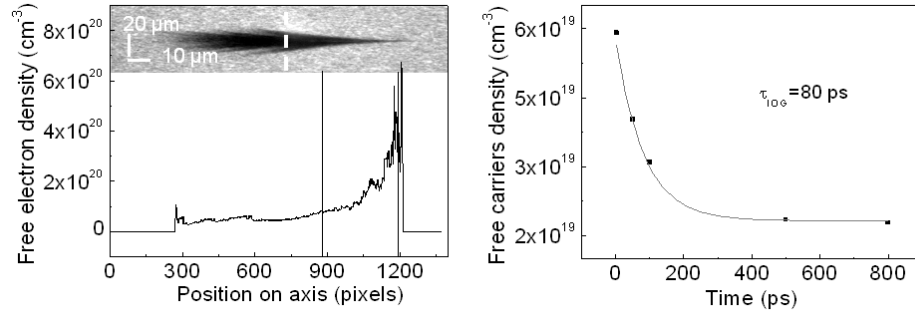

Figure 5.18: Same as Fig. 5.17 for an IOG-10 glass.

In order to estimate the decay rate of the free electron density, we choose arbitrarily a point on axis and follow the evolution of the electronic density in time. This point corresponds to the intercept of the optical axis with the dashed line in Fig. 5.17. The results are presented in Fig. 5.17. A fit (exponential decay, first order) over the data points reveals a free carrier decay rate of 8 ps in Bk7. The same evaluation is presented in Fig. 5.18 for IOG-10. Although the input energy has been kept constant with respect to the Bk7 investigation, the zone of energy deposition is more extended by a factor of about 2.

This difference in the energy deposition can be due to several reasons, for instance variations in the photoionization parameters, different plasma defocusing, or to a difference in the refractive index of the pristine bulk leading to different aberration effects. In IOG-10, the free carrier decay rate is estimated at a value of 80 ps.

5.6   Conclusion

In this chapter, we presented a setup of time-resolved microscopy allowing an in-situ observation of laser induced refractive index modifications in the bulk of transparent materials. The temporal resolution of the apparatus has been estimated at a value of 640 fs, and the spatial resolution is limited by the resolution of the optical microscope only.

The experiments with high laser pulse energies show the existence of an extended zone transiently modified. An in-depth study of this region illustrates the consequences of the free-carrier generation on the transient refractive index as well as the importance of self focusing during the pulse propagation. Furthermore, we could also visualize the effects of energy relaxation.

The analysis of the zone of permanent modification is facilitated when working with low laser pulse energies. As a main result, the microcavity visible after irradiation in a-SiO$_2$ coincides with a zone of strong thermal expansion. This indicates that thermomechanical effects play a dominant role, not only in BK7, as observed in Ch. 4, but also in a-SiO$_2$.

Finally, an application of this apparatus to the measurement of the free carriers lifetime in BK7 and IOG-10 is demonstrated. Decay times of 8 and 80 ps were respectively measured.